

Article

Landslide Investigation with Remote Sensing and Sensor Network: From Susceptibility Mapping and Scaled-down Simulation towards *in situ* Sensor Network Design

Gang Qiao ¹, Ping Lu ^{1,*}, Marco Scaioni ¹, Shuying Xu ¹, Xiaohua Tong ¹, Tiantian Feng ¹, Hangbin Wu ¹, Wen Chen ¹, Yixiang Tian ¹, Weian Wang ¹ and Rongxing Li ^{1,2}

¹ Center for Spatial Information Science and Sustainable Development Applications, College of Surveying and Geo-Informatics, Tongji University, Shanghai 200092, China; E-Mails: qiaogang@tongji.edu.cn (G.Q.); marco@tongji.edu.cn (M.S.); shadowice0810@163.com (S.X.); xhtong@tongji.edu.cn (X.T.); fengtiantian@tongji.edu.cn (T.F.); hb@tongji.edu.cn (H.W.); chenwen_ecnu@126.com (W.C.); tianyixiang@tongji.edu.cn (Y.T.); weian@tongji.edu.cn (W.W.)

² Mapping and GIS Lab, The Ohio State University, Columbus, OH 43210, USA; E-Mail: li.282@osu.edu

* Author to whom correspondence should be addressed; E-Mail: luping@tongji.edu.cn; Tel.: +86-189-1719-6131; Fax: +86-21-6598-5123.

Received: 5 August 2013; in revised form: 3 September 2013 / Accepted: 3 September 2013 / Published: 6 September 2013

Abstract: This paper presents an integrated approach to landslide research based on remote sensing and sensor networks. This approach is composed of three important parts: (i) landslide susceptibility mapping using remote-sensing techniques for susceptible determination of landslide spots; (ii) scaled-down landslide simulation experiments for validation of sensor network for landslide monitoring, and (iii) *in situ* sensor network deployment for intensified landslide monitoring. The study site is the Taziping landslide located in Hongkou Town (Sichuan, China). The landslide features generated by landslides triggered by the 2008 Wenchuan Earthquake were first extracted by means of object-oriented methods from the remote-sensing images before and after the landslides events. On the basis of correlations derived between spatial distribution of landslides and control factors, the landslide susceptibility mapping was carried out using the Artificial Neural Network (ANN) technique. Then the Taziping landslide, located in the above mentioned study area, was taken as an example to design and implement a scaled-down landslide simulation platform in Tongji University (Shanghai, China). The landslide

monitoring sensors were carefully investigated and deployed for rainfall induced landslide simulation experiments. Finally, outcomes from the simulation experiments were adopted and employed to design the future *in situ* sensor network in Taziping landslide site where the sensor deployment is being implemented.

Keywords: landslide; sensor network; susceptibility mapping; remote sensing

1. Introduction

Landslides are major geo-hazards heavily impacting many regions of the world in terms of human lives and economic losses [1]. The large magnitude of natural forces that are involved in landslides makes actions of mitigation or prevention unfeasible, with exceptions for small occurrences or under particular conditions. According to [2], on the basis of methods employed landslide research can be classified into theoretical, analytical and numerical studies along with laboratory experiments, field investigations, monitoring and inventory mapping, as well as GIS/Remote Sensing application.

Landslide assessment, susceptibility mapping, monitoring (*in situ* and remotely) and early warning systems all play an important role in landslide investigations thereby being directly related to disaster reduction and hazard mitigation. Remote sensing, especially from high-resolution satellite imagery is gaining importance in landslide investigation due to its wide coverage [3]. With its increasing spatial and temporal resolution, remote sensing has been widely adopted in landslide mapping for rapid response and recovery after hazard occurrence by government agencies as well as research community [4]. When data are available, the comparison of images collected before and after the event gives relevant support to landslide recognition [5,6]. Apart from its use in emergency response, when incorporated with other vector data the landslide inventory data from landslide mapping results and historical records can be employed as a database for susceptibility mapping using GIS and statistical approaches [7–9].

Landslide susceptibility mapping is an attempt to derive spatial variation of area-based slope failure probability or instability at a regional scale. This is based on a number of factors categorized into (a) preparatory factors such as lithology and geomorphology; and (b) triggering factors such as seismicity, rainfall, land cover, and anthropogenic causes. This technique is a fundamental tool for planners, administrators, and emergency managers, who are responsible for identifying hazard zones [10,11].

As another important component in landslide research, landslide monitoring has usually been regarded as a point-based and site-specific slope stability analysis [12]. In a broad sense, the term “monitoring” refers to the observations over time of any change in the area of interest caused by the landslide process. This includes either qualitative properties (vegetation cover, urbanization, land use, surface processes, and the like) or geometric aspects (deformation monitoring) [13]. Monitoring is, on one hand, a fundamental tool for understanding and modeling all geo-processes related to landslide dynamics. On the other hand, the integration of models and observations can lead to a greater opportunity for predicting partial or full slope failures. Monitoring also plays a major role in early-warning systems, where it should provide timely and reliable information to evaluate the present risk. The closer is the relationship between monitoring and modeling, the smaller is the uncertainty of forecasted events. Indeed, both tasks can mutually benefit through the assimilation of observation data and empirical or

physical models for the description of landslide behavior [14,15]. On one hand, dense and accurate observations can improve models. On the other, better models will help tailor the monitoring system to become more efficient in understanding geo-processes. This can be achieved, for example, by deployment of new sensors or by tuning the data acquisition rate according to the observed dynamics. In the latest generation of landslide monitoring systems, this capability to change the sensor parameters can be accomplished almost in an automatic way (“smart networks”). This, however, is a perspective of future development in this domain.

Landslides are complex geo-hazards requiring multiple observations to be investigated. For this reason, a large number of sensors could be installed as necessitated by the specific properties of each site. The term “sensor” is intended as in [16]. The logical connection between sensors is usually referred to as a “network”, within which sensors are the “nodes”. These nodes are implemented in a physical way using wired or wireless communication infrastructures [17] and different data transmission protocols [18]. In general, a Sensor Network (hereafter “SN”) can comprehend the different categories of sensors that are in use for gathering information about the underground layers, about the topographic of the slope surface, and about meteorological conditions. Usually these data inputs need to be updated at high-to-medium level of frequency (*i.e.*, from minutes to within a few days). On the other hand, some low-frequency data can be useful for the completion of the observation budget. Major categories of sensors include [19]:

- Geotechnical sensors to gather observations from surface and sub-surface;
- Geophysical sensors focusing on the underground layers;
- Surveying techniques (including the Global Navigation Satellite System, or GNSS—see [20]) which provide point-wise deformation measurements;
- Remote-sensing techniques (photogrammetry, laser scanning, and Interferometric Synthetic Aperture Radar (InSAR)—see [21–24]) that can offer “area-based” observations from different platforms (spaceborne, airborne and ground-based); and
- Environmental sensors, which can cover local (e.g., weather stations), regional (e.g., meteorological radars), and wide-areas (*i.e.*, meteorological satellites).

Monitoring should be complemented by up-to-date information on triggering factors, such as earthquakes [25] or anthropogenic activities [13,26] other than rainfall. The definition of a general methodology [27] for designing of a SN for monitoring landslides is a challenging issue that depends strictly on the geological processes involved [28], on the extent of the area under investigation, on the specific features of each site, and on the available economic resources. A detailed study of the local geological properties and the inventory of past landslides in the same region, as well as the acquisition of available information on past slope failures would significantly improve the model. In addition, information concerning the surrounding region (human settlements, hydraulic networks, communication infrastructures) and important targets (such as river barrages, energy power-plants and the like) is fundamental for designing risk scenarios outlining the serious impacts that could be caused directly by the landslide or by other domino effect such as the Na-Tech disasters [29,30].

2. Background of the Research

This research proposes a methodology for designing a SN, and its application to a landslide located in Sichuan province in southwestern China. Two important earthquakes (“Wenchuan” earthquake on

12 May 2008 [25] and “Ya’an” earthquake on 20 April 2013) have occurred in this area in the last five years, affecting different mountain locations. Both events were characterized by the triggering of several slope instability factors that, in the case of the 2008 earthquake, also coincided with intense rainfall resulting in floods and debris flows. In addition to the landslide runouts that occurred immediately after these earthquakes, many other slopes became unstable and represented a significant risk to man and property [31]. Considering the large area involved and the similarity between numerous unstable slopes (geometric properties, lithology, slope, soil, and ground coverage), the development of a unified, sustainable approach to landslide susceptibility mapping is quite important.

The key points of emphasis are: (i) the use of remote-sensing data together with some geo-referenced information from archives to determine the susceptible areas (see Section 5); and (ii) the construction of a scaled-down model of the slope to artificially reproduce the landslide process using a rainfall trigger (see Section 6). It is considered that future rainfall might be the highest probable triggering factor of new slope failures in the area [32]. The scaled-down model has two purposes. For one, it can be used to test the SN before it is deployed on the real slope [33]. In addition, it can provide observation results to be used in the process of numerical modeling of landslides.

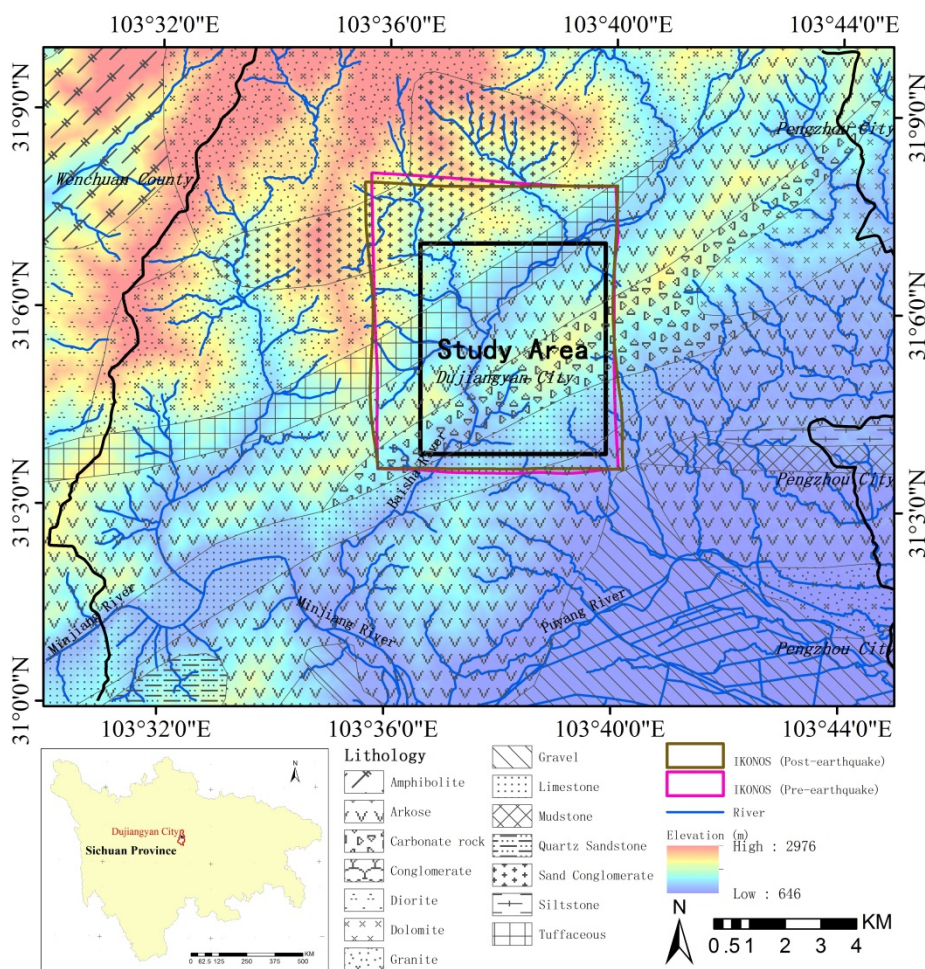
3. Research Area and Dataset

The research area is located in Hongkou Town (Sichuan, China) within the transition zone of the Chengdu Plain and the Western Sichuan Plateau. The approximate extent of the area is 30 km² and is characterized by relatively high and rugged mountains with elevations ranging from 700 to 1,700 m above sea level as well as deeply incised valleys [34] (Figure 1). This area is situated in the Yingxiu-Beichuan fault zone, where earthquakes and heavy precipitation lead to geological hazards such as landslides and debris flows, for example after shock events of 2008 Wenchuan Earthquake [31]. The major mountain range in this area is the Longmenshan Mountains, mainly composed of conglomerate, carbonat, tuffaceous, arkose, limestone, and granite rock (*cf.*, National Geological Archives of China, NGAC). The 2008 Wenchuan Earthquake triggered a large number of landslides, rock avalanches, and debris flows. Some of the landslides formed natural dams in the rivers, causing the potential secondary hazard of subsequent flooding. One third of the estimated 88,000 casualties of the earthquake were thought to be caused by landslides alone [35].

To map the landslides induced by the earthquake, two scenes of IKONOS imagery with almost the same coverage were used (Figure 1). The pre-event image was acquired on 14 September 2007, and the post-event one was taken one and a half months after the event on 28 June 2008.

In addition to this imagery, a DEM covering the research area having a grid resolution of 25 m × 25 m was provided by the National Geomatics Center of China (NGCC). Updated in 2011, this DEM is suitable to generate basic topographic information for landslide control factor analysis after the 2008 Wenchuan Earthquake. Updates of the road network and river data were obtained in 2011 from the Digital Line Graph (DLG) data offered by the NGCC. The lithology data and 2008-Wenchuan-Earthquake fault information were generated by the NGAC and the China Earthquake Networks Center (CENC), respectively.

Figure 1. Study area and profile of the data coverage.



4. Methodology

As shown in the flowchart (Figure 2), this study is composed of three parts: landslide susceptibility mapping for susceptible spot determination, a scaled-down landslide simulation experiment for SN test, and the *in situ* SN deployment of sensors for intensified observation of landslide activity. In the first part, landslides were extracted by means of an object-oriented method using the pre- and post-event IKONOS images. Then landslide control factors (including aspect, elevation, slope, lithology, distance to nearest river, distance to nearest road, and seismic intensity) were derived from the DEM and other vector data as listed in Table 1. The relationships between the distribution of the extracted landslides and the control factors were analyzed, and a landslide susceptibility map was generated based on Artificial Neural Network (ANN) to determine any susceptible spots (see Section 5 for details). In the second part, the Taziping landslide was selected as an example to design and implement a scaled-down landslide simulation platform at Tongji University (Shanghai, China). The landslide monitoring sensors were carefully investigated and deployed for this landslide simulation experiment triggered by rainfall, and conclusions concerning SN deployment were drawn. In the final part, current landslide prevention infrastructure and monitoring sensors were first introduced and discussed, and finally with the considerations from the simulation experiment, suggestions for future *in situ* SN deployment in Taziping were given.

Figure 2. Flowchart of the research approach.

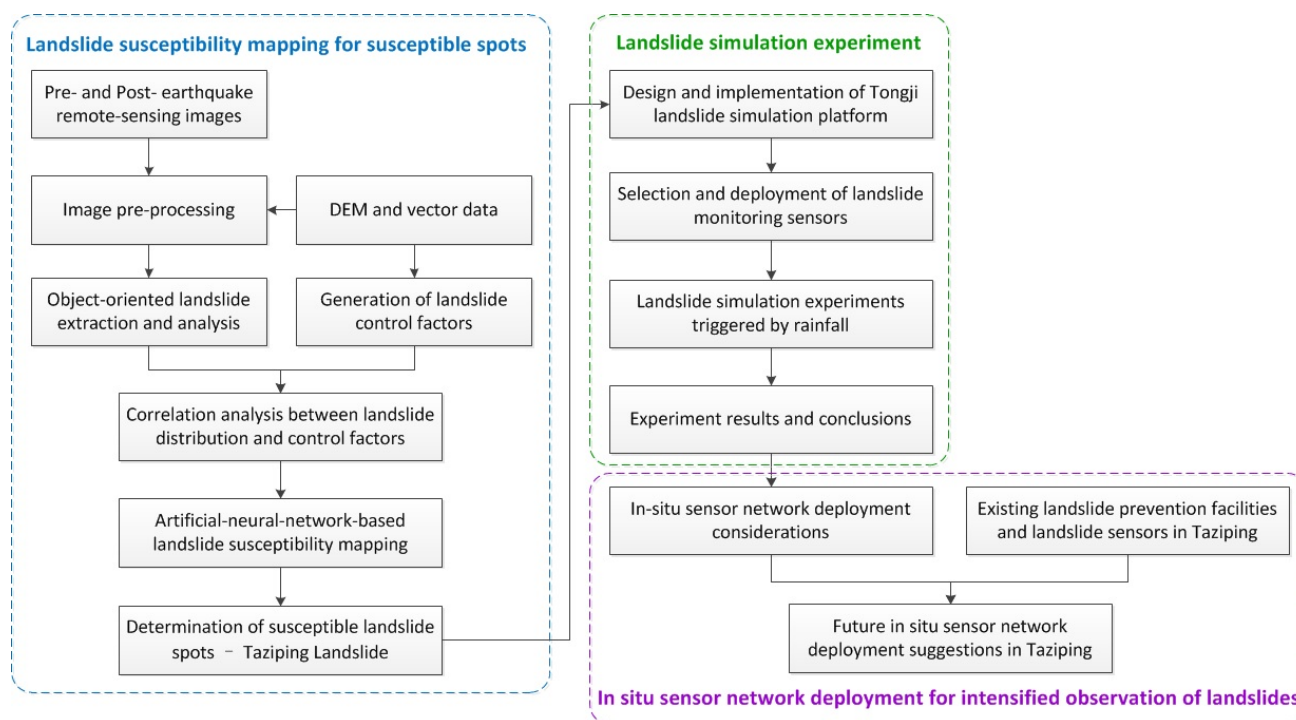


Table 1. Selected information on the IKONOS images and vector data used in the study.

Item	IKONOS Images		Vector Data				
	Pre-earthquake	Post-earthquake	DEM	Road	River	Lithology	Fault
Date	2007.9.14 12:12 pm	2008.6.28 12:02 pm	2011	2011	2011	2008	2008
Scale	NA	NA	1:50,000	1:50,000	1:50,000	1:500,000	NA
Resolution	1.0 m	1.0 m	25.0 m	NA	NA	NA	NA
Source	GeoEye Company (now DigitalGlobe)			NGCC		NGAC	CENC

5. Landslide Susceptibility Mapping

5.1. Landslide Extraction Based on Pre- and Post- Earthquake IKONOS Images

The IKONOS images were first enhanced, rectified and geo-referenced [36] based on the corresponding points obtained from vector data such as road networks, rivers, and land-use maps. Then an object-oriented approach [37,38] was employed to extract the earthquake-induced landslides. Since such geo-hazards usually occur on higher slopes and thus destroy the vegetation-cover, for most of the rugged mountains in this area any changes in vegetation-cover between the pre and post- event images could be viewed as landslide indicators [39,40]. A Vegetation Damage Index (VDI) is hence defined here and used for landslide recognition:

$$VDI = NDVI_{Pre} - NDVI_{Post} \tag{1}$$

where $NDVI_{Pre}$ is the Normalized Difference Vegetation Index (NDVI) [41] in pre-event image, and $NDVI_{Post}$ is the corresponding parameter in the post-event image.

A multi-resolution segmentation algorithm [37,42,43] was applied to the post-event IKONOS image to identify the homogeneous regions (namely “image objects”) and the $NDVI_{Post}$ value for each object

was computed. Then the image objects were overlaid with the pre-event IKONOS image to obtain the $NDVI_{Pre}$ values. An empirical threshold for the VDI of 0.36 was obtained after several trials based on visual inspection of resulting VDI map compared with observed landslides in the post-event IKONOS image in the research area. This value was used for the extraction of landslides from both images. Results were visually checked, and any errors (e.g., features such as roads sheltered by trees in the pre-event image and revealed in the post-event image, and some of the landslides with smaller VDI due to lower contrast) were edited to ensure the extraction accuracy by minimizing the number and area of the declassified landslides.

Figure 3. The landslides extracted from the two IKONOS images: (a) Landslide distribution overlaid on the post-event IKONOS and the river maps; and (b) A detailed landslide pattern (the outlined area in (a)) with a background of pre-event (upper) and post-event (lower) IKONOS images.

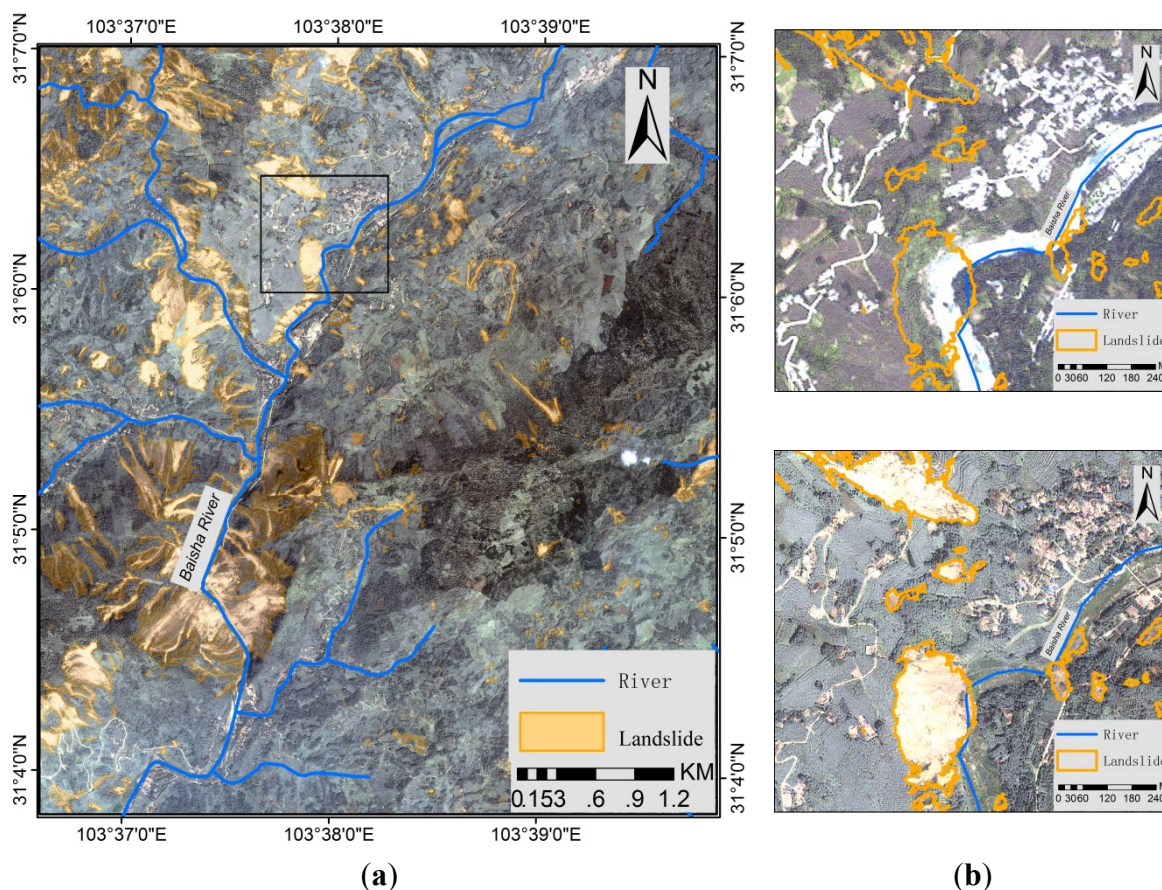


Figure 3a shows the extracted landslides overlaid on the post-event image as well as the river layer. In general, the landslide area shows dark brown contrast where it is compared with the nearby surroundings in remotely sensed images. The path of debris movement could be discerned easily, as the landslide resulted in newly denuded vegetation in comparison with the pre-event image [44]. The landslides were mainly situated on the hanging wall of the precipitous mountain ridges and on into the steep valley sides of the Baisha River and its tributaries. Most of the landslides took place in the western part of the study area with some very large ones in the southwestern section while only a few occurred in the eastern part where the terrain relief is relatively flat (see also Figure 4c). Figure 3b illustrates a detailed landslide pattern by the side of a village area with a background of the pre- and post- event

images to demonstrate the apparent changes caused by debris movement. Here it can easily be observed that some buildings were damaged, and a major trunk road was buried and blocked by a large landslide.

Table 2 shows the landslide numbers and area extracted from the remote-sensing images. For the IKONOS images having a 1.0 m spatial resolution, landslides with an area of less than 10 m² could sometimes be identified, but errors could also be introduced in this case, so they were removed from the statistics. In total, the extracted landslides cover a surface area of about 3.25 km², more than 10% of the research area, indicating severe damage by the landslides. The dimensions of individual landslide ranged from about 10 m² to more than 10,000 m². Most of the selected 740 landslides are with an area of 100–500 m², making almost half of the total number (41.62%), while a relatively small number (40) of large landslides (more than 10,000 m² in area) make the highest percentage (82.05%).

Table 2. Extracted landslide statistics in the research area.

Landslide Dimension (m ²)	Landslide Area		Landslide Number	
	Area (m ²)	Percentage (%)	Number	Percentage (%)
10–50	1,718.76	0.05	58	7.84
50–100	6,659.45	0.20	88	11.89
100–500	78,931.20	2.43	308	41.62
500–1,000	62,232.23	1.91	90	12.16
1,000–5,000	271,108.12	8.34	133	17.97
5,000–10,000	163,055.36	5.01	23	3.11
>10,000	2,667,869.77	82.05	40	5.41
Total	3,251,574.89	100.00	740	100.00

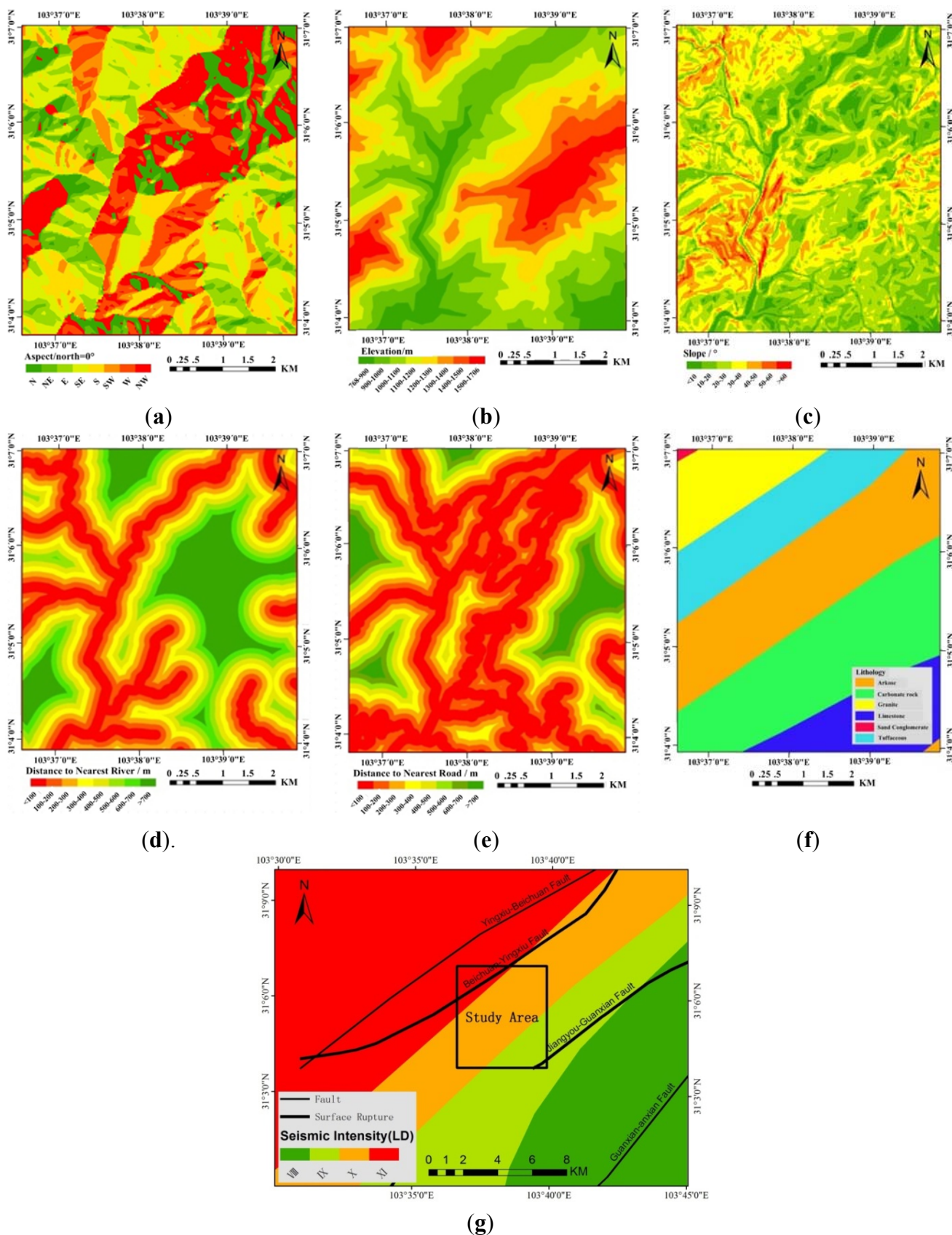
5.2. Correlation between Control Factors and Landslide Distribution

5.2.1. Generation of Control Factors

The control factors mentioned above are generally divided into topographical and geological factors [45,46]. In addition, seismic factors also are taken into account for earthquake-triggered landslides [47,48]. In this study, all three types of factors were considered. Topographical factors included aspect, elevation, slope, distance to nearest road, and distance to nearest river. The geological factor adopted was lithology. The seismic factor was the intensity of the 2008 Wenchuan Earthquake. It should be noted that the distance from the epicenter (approx. 30 km) was not used for this analysis because of the relatively small extent (approx. 30 km²) of the study area. This parameter would give a similar contribution in the whole region.

Figure 4 shows the landslide control factors in the study area: topographical (Figure 4a–e), geological (Figure 4f, lithology), and seismic (Figure 4g, seismic intensity). For the topographical factors, the aspect, elevation, and slope were derived from the DEM, and both the distance to nearest river and distance to nearest road were derived from the DLG data provided by NGCC. The lithology was generated from the 1:500,000 geological maps provided by the NGAC, and the 2008 Wenchuan Earthquake seismic intensity map was provided by the CENC.

Figure 4. The topographical (a–e), geological (f), and seismic (g) factors for landslides in the study area. (a) Aspect; (b) Elevation; (c) Slope; (d) Distance to nearest river; (e) Distance to nearest road; (f) Lithology; (g) Seismic intensity.



5.2.2. Correlation Analysis between the Control Factors and Landslide Spatial Distribution

In order to analyze the correlation between control factors and landslide spatial distribution, the former were first classified into different grades according to their specific characteristics and data ranges (see Table 3). The aspect factor was divided based on different direction classes with an amplitude of 45°. The elevation was classified based on 100-m intervals within the height range in the study area, while for the slope factor, classes of 10° were selected. For the distance-to-nearest-river/road factors, a 100-m interval was applied within the 700 m distance to obtain the grades. The lithology was classified on the basis of main rocks in the study area. The IX, X and XI seismic intensities (Richter scale) of the 2008 Wenchuan Earthquake were within the research area for further analysis.

Table 3. Detailed grades of the control factors used for correlation analysis.

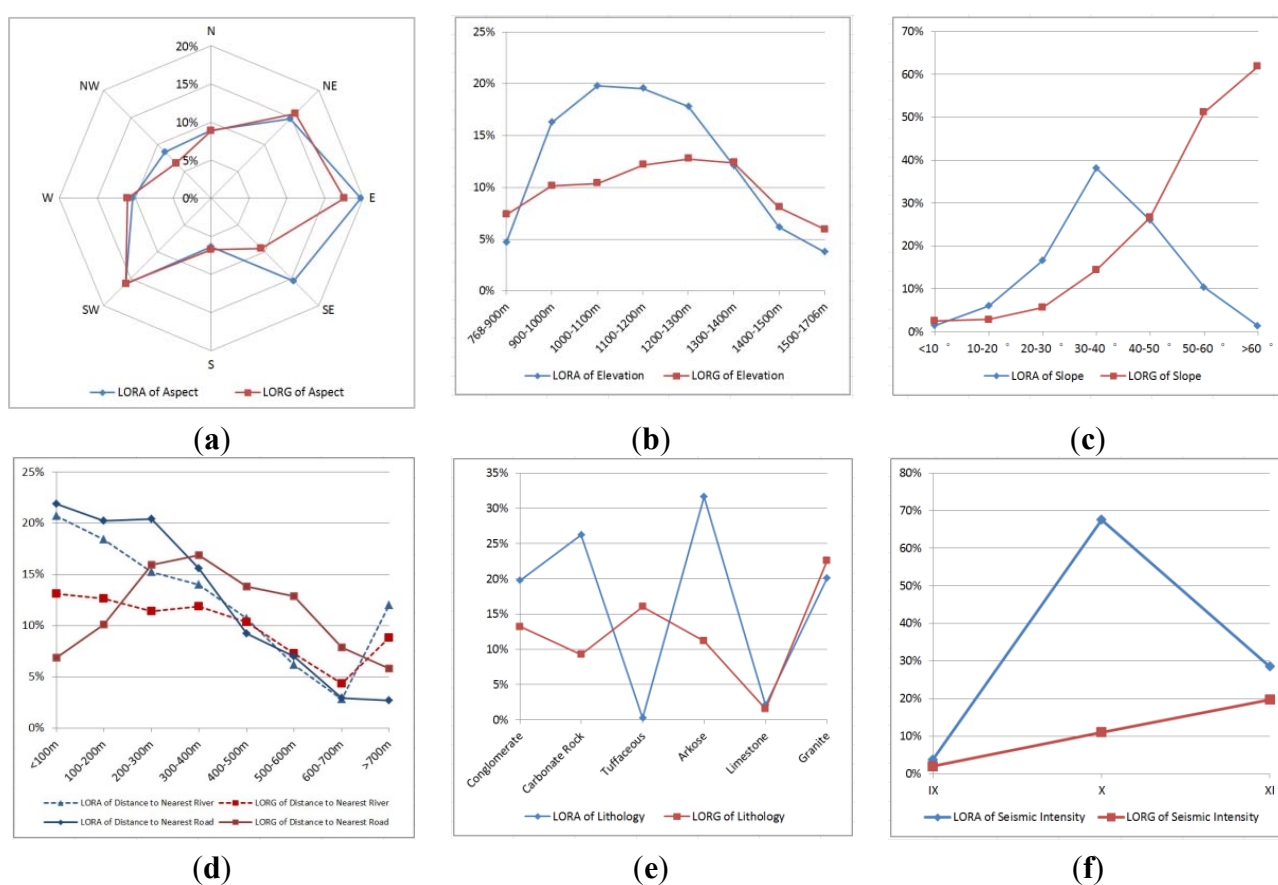
Grade	Aspect (°)	Elevation (m)	Slope (°)	Distance to Nearest River (m)	Distance to Nearest Road (m)	Lithology	Seismic Intensity
1	N	768–900	<10	<100	<100	Conglomerate	IX
2	NE	900–1,000	10–20	100–200	100–200	Carbonate Rock	X
3	E	1,000–1,100	20–30	200–300	200–300	Tuffaceous	XI
4	SE	1,100–1,200	30–40	300–400	300–400	Arkose	
5	S	1,200–1,300	40–50	400–500	400–500	Limestone	
6	SW	1,300–1,400	50–60	500–600	500–600	Granite	
7	W	1,400–1,500	60–68	600–700	600–700		
8	NW	1,500–1,706		>700	>700		

On the basis of this dataset, two parameters were determined for analysis of the correlation between landslides and control factors: (1) Landslide Occurrence Rate in All landslides (LORA) and (2) Landslide Occurrence Rate in a certain landslide Grade (LORG) [49]. The former can be defined as the ratio of the landslide area within a certain grade with respect to the total landslide area extracted from satellite images of the area. The latter is the ratio of the landslide area within a certain grade to the area of this grade in the research region. LORA represents the percentage of the landslide area in a certain grade, while LORG denotes the possibility of landslide occurrence for a certain grade within the study area.

Figure 5 shows the correlation between landslides and the control factors with the blue line representing the LORA and the red the LORG. For the aspect factor, the values of both LORA and LORG are similar in the research region, and the two indexes are higher in the NE, E, SE and SW than in other directions, revealing that there are more landslides occurring in these directions. For the elevation factor, the LORA value (landslide area) is larger in the elevation range of 900–1,400 m, but the LORG is relatively smooth for all the grades, indicating no obvious correlation in elevation factor. For the slope factor, the LORA first increases and then decreases with the summit at 30°–40°, indicating the larger landslide area within the middle of the slope angle range, while the LORG ascends along with the rising slope angle, showing clear dependency between the landslide possibility and the slope angle and that higher slope areas are more unstable for the occurrence of the earthquake-triggered landslides. For the distance-to-nearest-river/road factors, a similar trend could be viewed for the LORA lines, and both values decrease progressively as the distance increases, showing that more landslides occurred near the rivers or roads. For the LORG lines, the distance-to-nearest-river [50] value has a similar

depression tendency, indicating that the landslides occurred easily in valleys with flowing rivers. The distance-to-nearest-road value shows an increasing and then decreasing curve with the maximum in a range of 200-to-500 m, which is most probably due to the fact that roads are built mainly within this distance to mountains having a slope of 30°–40°. For the lithology factor, the landslides occurred mostly in regions of arkose and carbonate rock, while granite and tuffaceous are rocks most vulnerable to earthquake-triggered landslides. As to the seismic intensity factor, the X degree takes most of the landslide area, while possibility of landslides increases with the seismic intensity from IX, X to XI. This is consistent with common knowledge.

Figure 5. Relationships between landslides and the control factors: aspect, elevation, slope, distance to nearest river/road, lithology, and seismic intensity. (a) Aspect; (b) Elevation; (c) Slope; (d) Distance to nearest river/road; (e) Lithology; (f) Seismic intensity.



5.3. Landslide Susceptibility Mapping Based on an Artificial Neural Network

Landslide susceptibility mapping will provide an effective means for determining the susceptible regions for landslide monitoring. Landslide susceptibility mapping is commonly used in landslide research and prediction [51–53]. As a widely used non-linear method of prediction, the Artificial Neural Network (ANN), which is a generalization of mathematical models to simulate the human cognition and neural biology and thus to predict outputs from inputs [54], was employed in this research to derive the landslide susceptibility map. ANN has been recently used in landslide susceptibility mapping, and was proved to be an effective means for landslide prediction due to its capability to establish the complex and non-linear relationships between landslide distribution and the control factors [11].

In a typical landslide susceptibility mapping application, the ANN is usually composed of three steps: training, validation, and susceptibility mapping [55,56]. A back-propagation learning algorithm, consisting of input layer, hidden layers, and output layer was used to train the ANN in this research. The back-propagation algorithm is a procedure that minimizes the Sum of Squares for Error (SSE) in output layer by modifying the weights of ANN parameters to approximate the input sample and output sample. This multi-layer back-propagation algorithm was selected in this paper because it is one of the most commonly used ANN models that has the advantages of non-linear mapping, self-learning, and fault tolerance with respect to other models [57].

The landslides extracted from the IKONOS images were randomly divided into two groups, one used for training the ANN, and the other for accuracy assessment. The training sites were selected based on analysis of the topographical (aspect, elevation, slope, and distance to river/road), geology (lithology), and seismic (seismic intensity) landslide control factors. Based on the analysis described in the previous section, the LORG index of the control factors was used as the standard inputs for the network training due to its more reasonable evaluation compared with LORA, and the outputs of the training were the spatial distributed landslides extracted from satellite images. We tested different training methods, including the improved back-propagation algorithms and the numerical optimization based techniques, and found that the Levenberg-Marquardt approach featured the best performance in terms of Mean Square Error (MSE) [58,59], So it was selected in the back-propagation algorithm to calculate weights between the input layer and the hidden layer, as well as between the hidden layer and the output layer, by modifying the number of hidden layers and the learning rate [60] (see Table 4). The activation function in the hidden layer was set to tansig, and that in the output layer was set to purelin [58]. The input node (neuron number) was set to seven for the corresponding control factors and the output node (neuron number) was set to 1 for the susceptible value. The neuron number in the hidden layer was determined to be nine by evaluation of the training time, iterations and the resulting SSE (see Figure 6). 80% of the landslides were randomly selected as training data for the ANN, and the remainder was used as check points to validate the accuracy of the susceptibility mapping. Finally, with 58 iterations, an MSE (Mean Square Error) of 0.308 was achieved for the Levenberg-Marquardt method, and an accuracy of 95% could be reached for the assessment.

Table 4. The Weights of the Artificial Neural Network (ANN) Parameters (Levenberg-Marquardt method).

Network Parameters	Weights
Learning Rate	0.05
Threshold of Residue	9.5238×10^{-4} , or SSE = 0.02
Error Increase Factor	1.04
Minimum Gradient	1×10^{-10}
Number of Maximum Training	2,000

The landslide susceptibility map derived from the ANN is shown in Figure 7, where the level of susceptibility was divided into five categories according to the output value r : very low ($r < 0$), low ($0 \leq r < 0.25$), moderate ($0.25 \leq r < 0.5$), high ($0.5 \leq r < 0.75$), and very high ($r \geq 0.75$). The overlay rate between the extracted landslides and the ones predicted by the susceptibility map is 89%, indicating the high reliability of the ANN approach.

Figure 6. Mean Square Error (MSE) vs. neuron number in the hidden layer (Levenberg-Marquardt method).

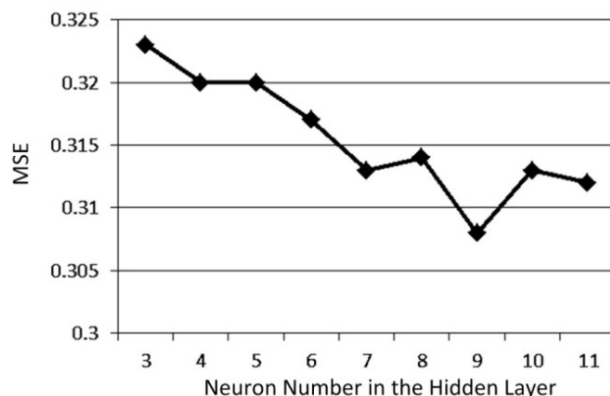


Figure 7. Landslide susceptibility map derived from Artificial Neural Network (ANN) (Levenberg-Marquardt method).

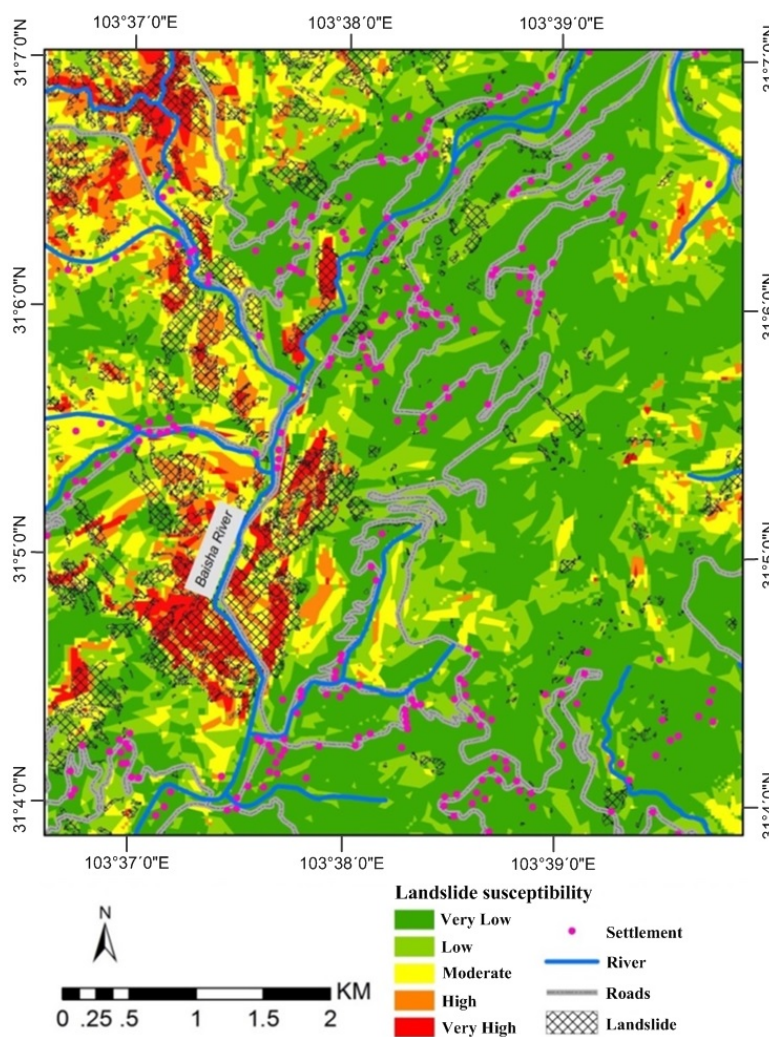


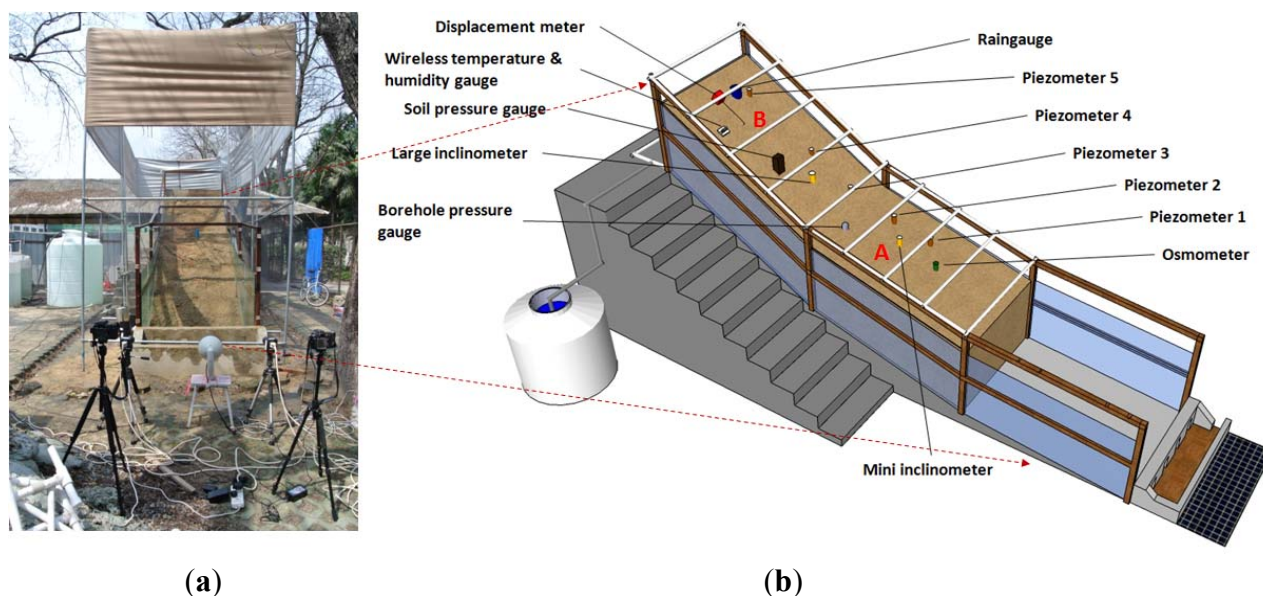
Figure 7 shows that the more landslide-prone regions are located mainly in the rugged mountainous areas having high slopes. The western and the northwestern areas are those most commonly susceptible to landslides, and there are relatively fewer settlements in these regions. One of the most susceptible spots, Taziping, was selected for landslide monitoring based on an *in situ* geo-sensor network because

there is a river flowing nearby, and because there are relatively densely populated settlements in the area (Figure 7) which could be severely damaged if a landslide occurs. Before deploying sensors in the field of Sichuan, a scaled-down landslide simulation and monitoring system was constructed on the campus of Tongji University to test the usability and deployment strategy of these *in situ* sensors. The simulation experiment is detailed in the next section.

6. The Scaled-Down Landslide Simulation

A simulation platform can be used as a first step in defining the set of *in situ* sensors to be adopted in the field. In addition, it can be used to understand the data interpretation and processing approach. For these purposes, a scaled-down landslide simulation platform (Figure 8) has been set up on the campus of Tongji University. The main purpose of this facility is to test the potential of various sensors in detecting early-warning signals.

Figure 8. The scaled-down landslide simulation platform on the campus of Tongji University (a) and the spatial distribution of *in situ* sensors for the experiment (b).



This scaled-down landslide simulation experiment system is composed of a simulation platform of mass movement, a spatial SN, a data collection and communication sub-system, a data storage server, and a visualization system [33]. Firstly, the simulation platform was designed to simulate the movement type, the geological configurations, and the triggering factors of intensive rainfall for the real-scene landslide that occurred in Taziping, Sichuan Province. Secondly, the SN includes a set of contact and non-contact sensors that were installed for observing and measuring different types of parameters that are related to landslide initialization, reactivation, acceleration, and, finally, failure of the slope. Thirdly, the data collection and communication sub-system was composed of the following components: (1) a data taker (dataTaker[®], DT80) to collect data from all the contact sensors and then wirelessly transfer the signals through a General Packet Radio Service (GPRS) network; (2) a serial-port sever to gather some of the non-contact sensors and then transmit to the database server through 3G service, and (3) a self-organizing and self-healing mesh network to collect and transfer the video stream in real time through an iMesh device developed by the OTEC Communication Technology Co. (Guangzhou,

China) [61]. Fourthly, the data storage server receives data from the wireless network and then interprets and stores this data for different sensors into different categories of the database. Finally, a visualization system composed of nine screens (46 inches each) was installed in the monitoring headquarters. This can instantly visualize the sensor positions, real-time video stream of mass movement, 2D spatial distribution of piezometers, temporal readings of sensors and the status of different sensors.

To simulate the Taziping landslide, the platform dimensions were designed to be 1.5 m in width and 6 m in length. The platform was divided into three equal sections having slope angles of 5°, 15°, and 30°, respectively. Tempered glass windows framed in steel in both sides of the platform were fixed to hold the landslide mass, and for the visual observation of the internal changes. To simulate the rainfall-triggered landslide, an artificial precipitation system was installed at the top of the landslide body. This system is composed of a water tank of 3,000 L in volume for the water supply, a pump to lift water for rainfall, and five evenly distributed water sprays that can be controlled and manipulated for precipitation duration and intensity. In addition, a steel frame was constructed to support a water-tight canvas enclosure to keep the sprayed water within the landslide body.

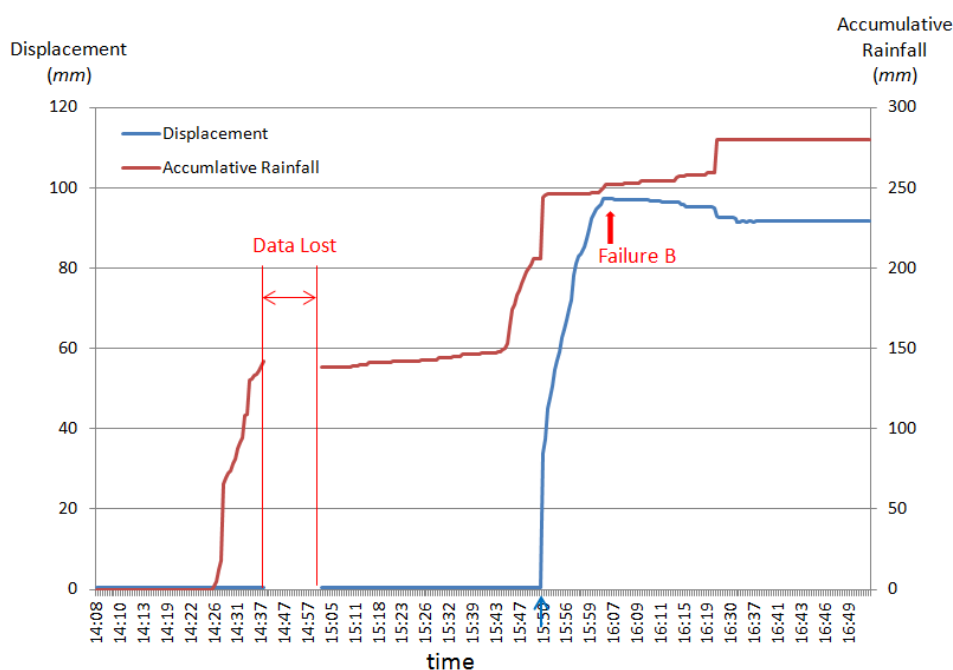
In this experiment, a total of 13 spatial *in situ* sensors were deployed (Figure 8). These sensors were used mainly to monitor landslide characteristics and triggering factors such as surface displacements on the landslide body, slope inclination, pore water pressure of groundwater flow, rainfall intensity, soil pressure, acceleration of slope movement, *etc.* For example, five piezometers were aligned along the sliding direction at the bottom of the landslide body with a depth of 1.5 m so as to interpret the changes in pore water pressure before and after slope failure. However, due to the limitations of scale, some sensors that will be used in the field, such as the GNSS, are not meaningful in a scaled-down model, so these kinds of sensors were not tested for the experiments. In addition to *in situ* sensors, in order to observe the surface displacement and landslide failure process and to evaluate the landslide magnitude, some stereo-camera systems and 3D imaging sensors were integrated into the simulation platform. Technological aspects that should be tackled on the real-scene landslides require a more in-depth analysis before moving from the simulation platform to the field.

Two technological issues need to be better focused before illustrating the results from the simulation experiments. The first concerns the use of wired connections between each contact sensor and the corresponding data acquisition unit (chiefly the data Taker[®]), which seems to contradict the use of a Wireless Sensor Network (WSN). For real-time field applications, the use of clusters of sensors has been devised to be the optimal solution to coping with the following problems. First, a solar power supply (consisting of a solar panel and its control and storage unit) can be shared among a large number of sensors; based on this hypothesis, power cables would be required for energy supply, and thus can be used for data communication as well. A local acquisition unit can be located close to the power source and operate for the entire sensor cluster; the successive communication from the local control unit to a central control unit outside the field then can be based on wireless technology. From this point of view, the simulation platform reproduces a sensor cluster. Second, the deployment of several sensors in a neighborhood allows for the cross-validation of spatially correlated observations. The second technological concern is related to the use of oversized communication channels. This selection is motivated by the required scalability of the SN, which should be able to accommodate a variable number of sensors under the same network structure.

The significant number of sensor observations was derived from the rainfall induced-landslide simulation experiment conducted on 18 November 2011. This experiment started at 14:08 and lasted about 2 h and 40 min. Due to a wireless communication technical problem, there was a period of data loss lasting for 25 min (14:37–15:02). The experiment was performed under the simulation of an intensive rainfall of approximate 280 mm within 3 h (as recorded by the rain gauge), with two periods of extremely heavy rainfall (14:25–14:40, 15:40–15:50) (Figure 9).

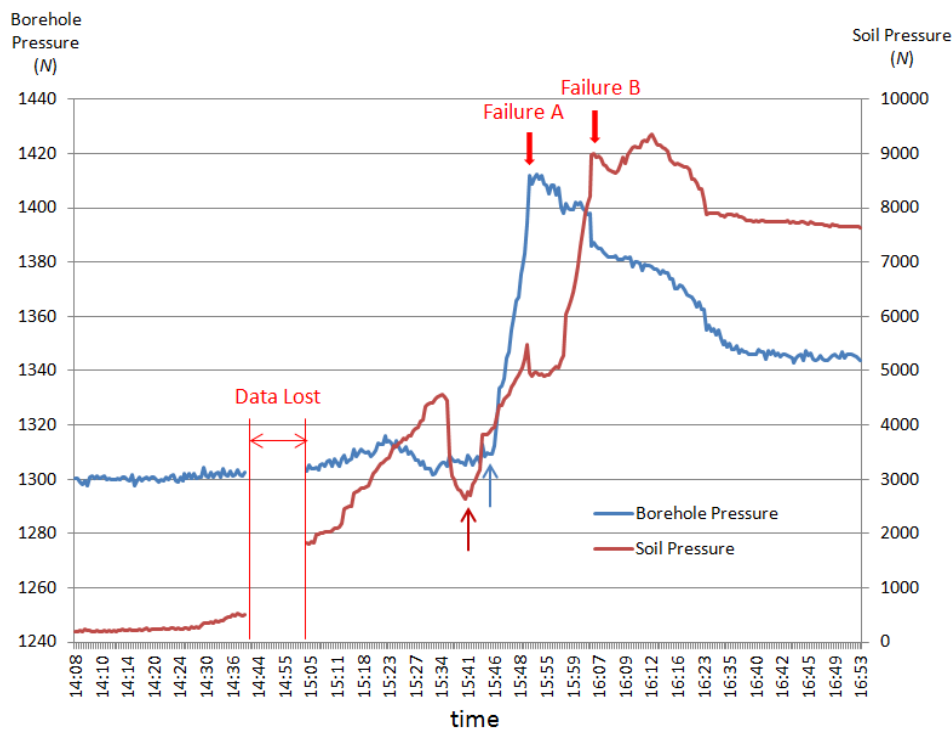
The flume test for a simulated landslide always renders the research concern on the rainfall condition, which necessarily needs a consideration of the field site and the amount of rainfall to trigger the slope failure in the experiment. As a result, it is necessary to set rainfall conditions that can evaluate the relationship between actual rainfall amount in the field and slope failure during the flume test. The regional area where the Taziping landslide is located is along the seismic zones that were strongly affected by the 2008 Wenchuan Earthquake. In this area, the amount of rainfall necessary to trigger landslides and debris flows nevertheless has not been well studied by previous researchers. [32] reported an accumulative rainfall of approx. 330 mm in 40 h (23–24 September 2008) which induced 969 new landslides in this seismic region. In our simulation, a rainfall accumulation of 280 mm over 3 h was used, with higher hourly rainfall intensity than the actual amounts in the field. The reason for using higher rainfall intensity during the experiment was to include the consideration of landslide scale. The simulated landslide is at a much smaller scale than the real-scene landslide. To match the scale, the rainfall simulation facility has been designed to produce decreased sizes of raindrops and increased density of raindrops. This is also the reason why natural rainfall is not used in the experiment considering its larger size of raindrop. In terms of the applied tipping bucket rain gauge with the same diameter (203 mm) of cylindrical container, it records higher rainfall intensity for dense, small-sized raindrops. This does not indicate that the measurements from the rain gauge are not correct, but it reflects the fact that in order to simulate the same effect of rainfall as in the field, a scaled rainfall simulation system with higher rainfall intensity is needed.

Figure 9. Monitoring data from the rain gauge and the displacement meter.



The first slope failure started from the bottom of the landslide body (Figure 8) at 15:50. This was observed by the borehole pressure gauge mounted at the bottom of the landslide with a depth of 1.5 m (Figure 10) and the mini inclinometer (Figure 11) set up in the lower part of the slope with a depth of 0.5 m. These gauges detected significantly increasing signals starting 5 min and 20 min, respectively, before the failure in section A. A subsequent slope failure occurred in the upper part of the slope at 16:05. This was recorded by the soil pressure gauge installed just below the slope surface (Figure 10), the displacement meter put on the slope surface (Figure 9), and the two-axis large inclinometer covering the whole depth of the landslide (Figure 11). These gauges noted a sudden signal change 25 min, 15 min and 20 min, respectively, before the failure in section B. In addition, the mass movement can be noticed 20 min before the initial failure by changes in the pore water pressure (Figure 12) that were measured by an osmometer and a set of piezometers affixed to the bottom the landslide body with a depth of 1.5 m.

Figure 10. Monitoring result of the borehole pressure gauge and the soil pressure gauge.



While the high-resolution cameras provide images throughout the entire duration of a simulation experiment, high-speed cameras are used mainly to analyze the final slope failure, which might feature very rapid movements. Both camera systems gather sequences of stereo images to be used for photogrammetric analysis (volume computation, surface point tracking); at the moment, these processing tasks are applied after the end of the experiment, in a manner similar to how satellite remote-sensing observations will be used in field applications. On the other hand, the high-speed camera system could be used for both tasks after selection of the most suitable time span of the images to process for each part of the experiment.

Figure 11. Monitoring data from the two-axis large and one-axis mini inclinometers.

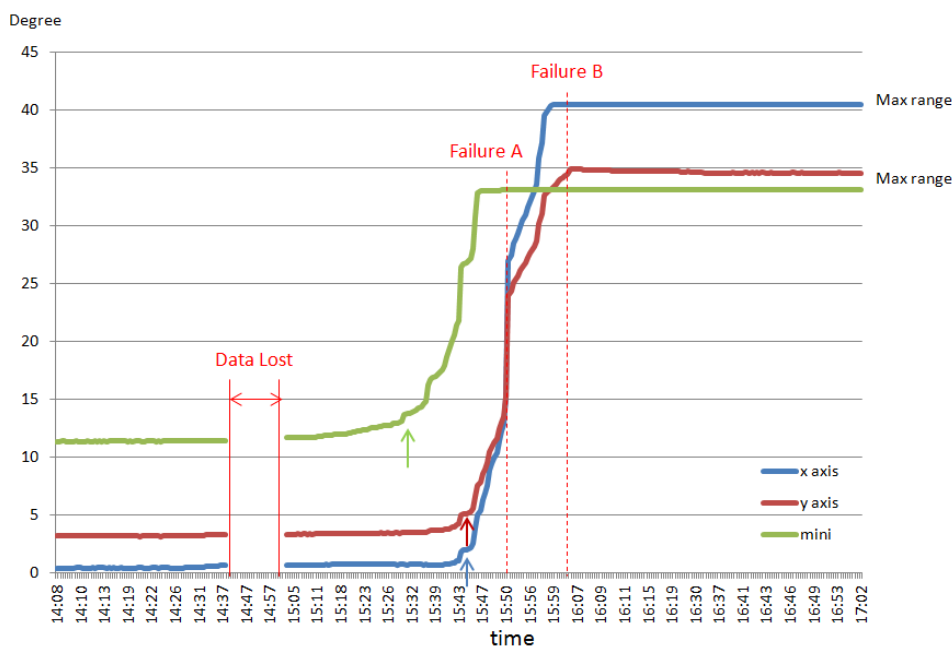
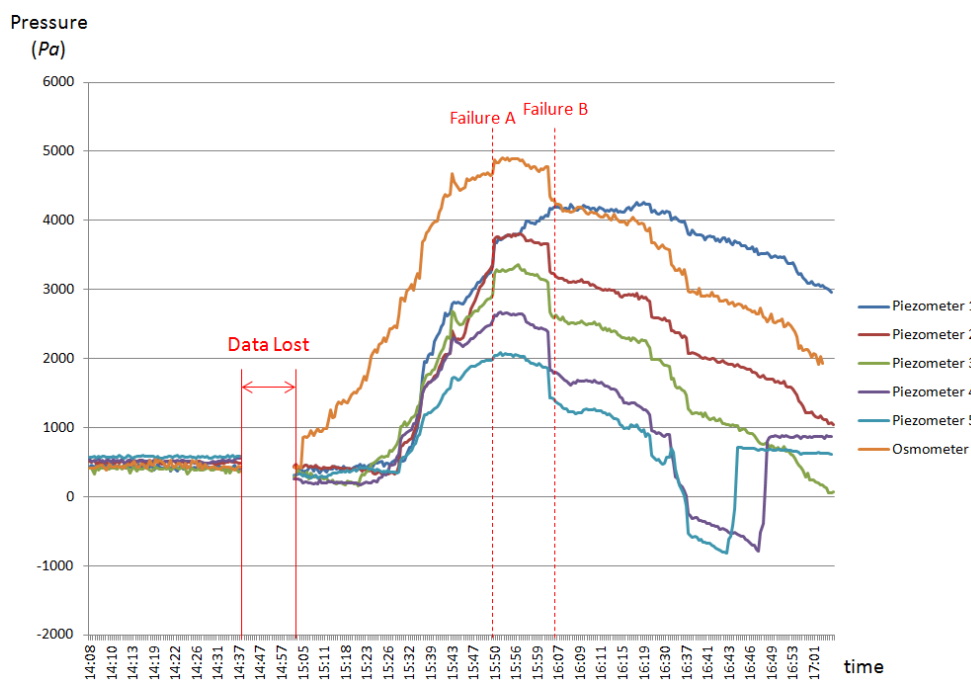


Figure 12. Monitoring data collected by the osmometer and the piezometers.



In recent years, several 3D imaging sensors have been introduced that can provide the direct acquisition of a 3D surface by means of phase-shift analysis (range cameras) or by using triangulation principles [62]. Although the resolution and precision are lower than the ones obtained from the above-mentioned photogrammetric systems, they would allow for real-time processing.

In a nutshell, the above-mentioned landslide simulation experiment confirms the usefulness of *in situ* sensors (such as inclinometers, piezometers, borehole, and soil pressure gauges) in real-time landslide monitoring and detection of early-warning signals. These sensors can be further employed reliably in real-scene landslide monitoring in Taziping, Sichuan Province, China. In addition, the experiment

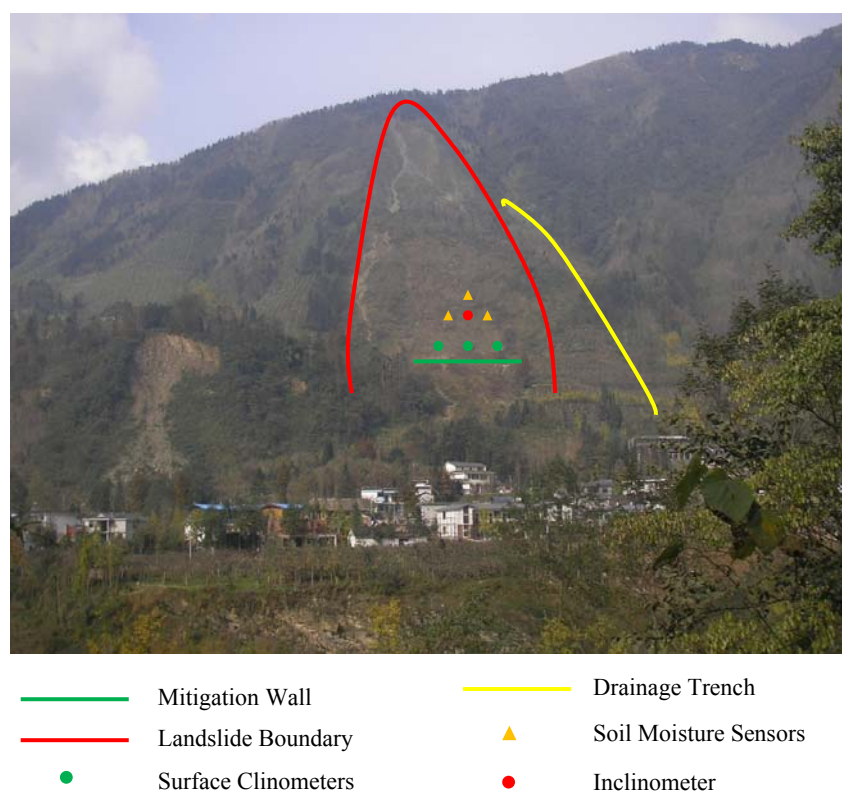
shows the possibility of transferring real-time video streams from the infrared video camera through a wireless network. As new approaches for landslide monitoring, high-speed stereo cameras and 3D imaging sensors can provide alternative means for landslide stability evaluation through remote-sensing approaches. However, due to scale differences and field conditions, they need to be further tested and evaluated in the field for real-scene landslide monitoring.

7. In Situ Sensor Network Deployment in Taziping Landslide

7.1. The Existing Landslide Prevention Facilities and Monitoring Sensors

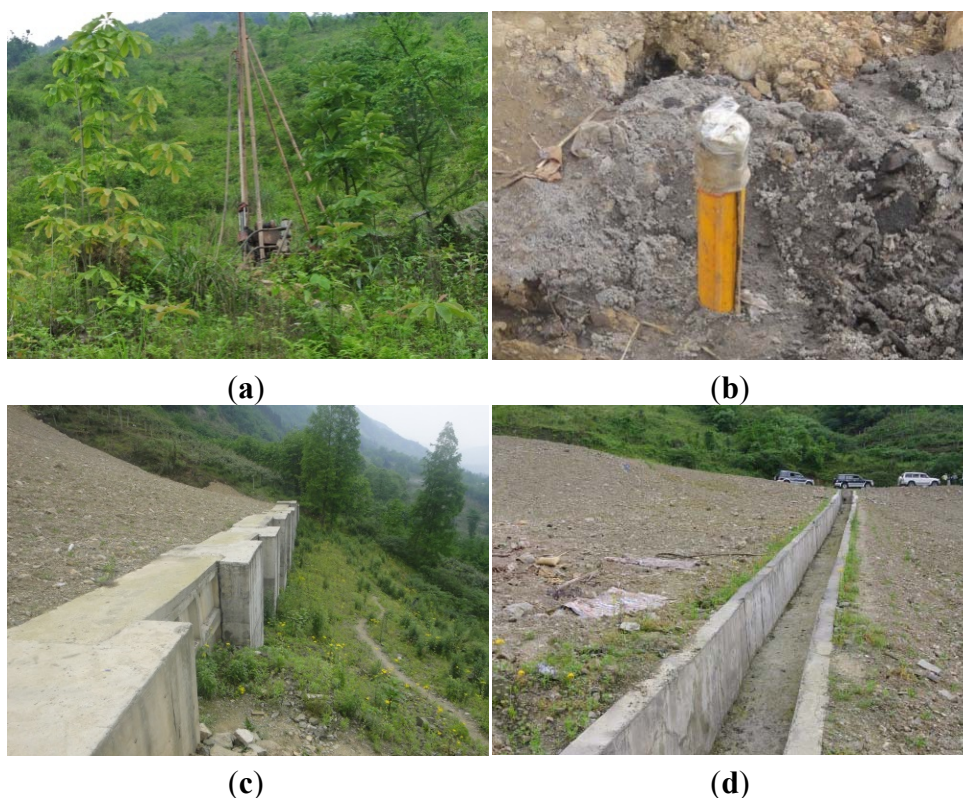
The Taziping landslide (Figure 13) is located above Hongkou Town, which was strongly affected by the 2008 Wenchuan Earthquake. The elevations of the source and the toe areas are about 1,370 m and 1,007 m, respectively, with a relative elevation difference of about 363 m. The slope ranges from 25° to 40°, with relatively steep landslide source areas and a relatively flat toe of mass accumulation. After the event, the landslide was frequently accelerated by intensive rainfall and subsequent water infiltrations, especially with the accumulation of loose debris and the fragile soil characteristics triggered by the earthquake [32]. Due to the extensive amounts of loose debris carried from the source areas, this landslide has the potential to turn into debris flows with intensive surface water adjunction. In addition, frequent human activities such as road building, forest cutting and fruit cultivation can often further decrease the stability of the slope and accordingly accelerate the sliding processes. The Taziping landslide represents a major threat to the town at the foot of the mountain not only in terms of human lives, but also in terms of infrastructure and local economic development.

Figure 13. An overview of the Taziping landslide, the mitigation infrastructure and the currently available sensors for monitoring.



Due to the high vulnerability of the slope, since 2010 the Taziping landslide has been continuously reinforced by the constructions of mitigation infrastructure. Efforts include the positioning of anchors, mitigation walls, shallow drainage trenches and a system for surface water run-off (Figures 13 and 14). In order to monitor the effectiveness of these mitigation efforts, three types of preliminary sensors have been installed on the landslide. First, a MEMS (Micro-Electro-Mechanical Systems) inclinometer with a depth of 15 m has been set up in the middle of the slope to measure the sliding surface and evaluate the activeness of the landslide. Second, three surface clinometers were established close to the mitigation wall in order to measure the surface displacement of the slope and evaluate the effectiveness of the mitigation program. Third, for the purpose of measuring ground water, three soil moisture sensors were mounted close to the surface drainage system. Although these sensors provide a useful approach to monitor the status of the slope, the system does not provide the possibility for real-time transfer of acquired data and it requires frequently manual readings of data collected by *in situ* data collection units. As a result, a more sophisticated real-time monitoring system is needed.

Figure 14. Some existing facilities and sensors at the Taziping landslide: (a) Installation for soil moisture sensor; (b) Inclinometer; (c) Mitigation wall; and (d) Drainage trench.



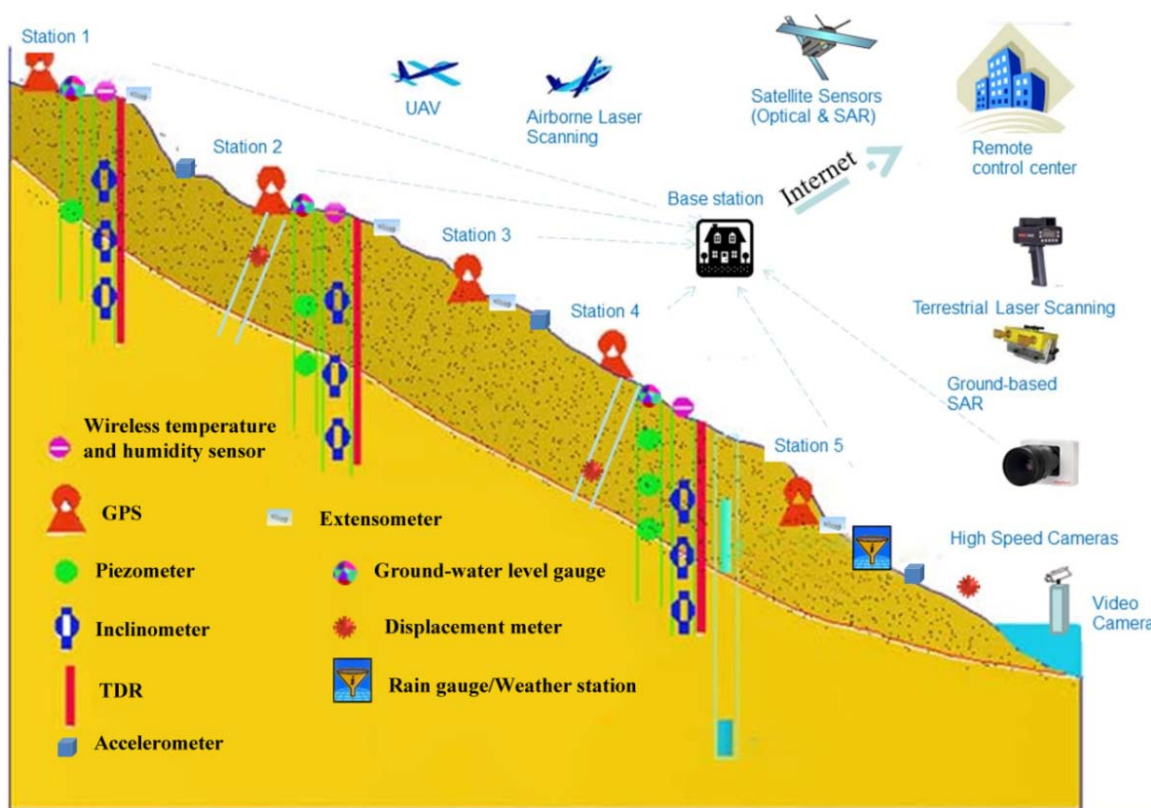
7.2. Design Considerations for Future Sensor Network Deployment at the Taziping Landslide

The SN tested in the landslide simulation experiment was successful in the following aspects. First, it enabled a rapid data transferring from the landslide to the monitoring headquarters in real time, which satisfied emergency management requirements when the slope is approaching failure. Second, a combination of three communication approaches (GPRS, 3G and broadband) separated different types of data and thus avoided transfer congestion at a single data node. Third, the experiment showed that a network-based monitoring system is more reliable than a point-based strategy because sensors can work

collaboratively and cross-validation of data reliability is made possible. Fourth, the networked sensors ensure the transmission efficiency and accordingly avoid great delay of data transferring and storage. Finally, the experiment encompasses a complete and sophisticated monitoring system that includes *in situ* SN, data collection units, diverse communication approaches, data processing and storage units, and a visualization system.

Such a system will be transferred in the future to real-scene landslide monitoring in Taziping. A preliminary design of the improved network is sketched in Figure 15. The plan of this network is to use five communication relay stations on the slope of the landslide, each of which serves as a gateway node, namely working as a local data collection unit and as an intermediate point for data distribution and communication. These five stations are designed to form a connected SN, provided that the data communication between them can be maintained. If there are significant obstacles (e.g., forests) which block communication routes, more stations will be established, with each installation maintaining a certain distance above the ground. Each station will apply a multi-hop device for fast roaming communication that allows for a fast shift (within 0.01 s).

Figure 15. Design of the spatial sensor network to be deployed at the Taziping landslide.



For each sensor node of the station, a series of sensors will be connected for local data storage and distribution. Inside the drilled borehole, piezometers will be installed to monitor changes of pore water pressure in the ground water, especially for real-time monitoring of water infiltration after an intensive rainfall event. Also, inclinometers will be assembled and then installed inside the slope so as to measure slope movement both vertically and horizontally. Each gateway node also will include an extensometer that measures surface displacement. In terms of a rainfall triggering factor, a rain gauge will be used to monitor accumulative rainfall in real time. By employing a weather station that takes advantage of the

National Oceanic and Atmospheric Administration (NOAA) weather forecast model [63], it is possible to forecast rainfall levels within 12 h, thus allocating the monitoring priority to the rain gauge and the weather station. These sensors were well tested during the landslide simulation experiment and can reach expected results for landslide monitoring.

In addition, the following sensors have been considered for more comprehensive observations. Time Domain Reflectometry (TDR) is to be installed to detect internal fractures of the slope. In the meanwhile, it can measure the level of ground water, providing comparisons for the observations from the piezometers. In addition, plans call for mounting high-frequency (80 Hz) accelerometers to be used for detecting surface vibration caused by the mass movement and, subsequently, for evaluation of the amount of acceleration. If the satellite signals can be received, GNSS then can be added as a ground reference for measuring surface displacement. Besides *in situ* sensors, certain remote-sensing platforms are scheduled to be installed. A ground-based InSAR [64,65] will be installed at the toe of the landslide so as to scan the entire slope and measure surface displacement along the Line-Of-Sight (LOS). Moreover, a pair of stereo high-speed cameras has already been tested and will be employed to capture the moment of slope failure so as to further analyze the landslide mechanism especially during the critical moment of slope failure. Since topographic information concerning a slope is fundamental for further analysis of landslide process, a long-range terrestrial laser scanning system [66] is to be put at the foot of the mountain so as to obtain a high-resolution DTM of the slope and, with multi-temporal acquisitions, to measure the surface displacement from both cloud points and sequential DTMs. The point clouds can also be acquired from airborne laser scanning [67], which allows for a larger scanning extent useful for regional analysis. Owing to its flexibility and low cost, it is planned to employ a Unmanned Aerial Vehicle (UAV) [68], embedded with a high-resolution camera, to acquire high-resolution aerial photos, to detect small rock fissures of the slope, and to generate a DTM for comparison with that formed from laser scanning. Finally, based on the satellite platforms, the ground movement can also be well detected using InSAR [69], especially for shorter wavelength sensors such as TerraSAR-X and COSMO-SkyMed, which allows a detection precision of millimeters.

Nevertheless, for a successful transplantation of the SN from the simulation platform to the *in situ* environment, careful consideration still needs to be made, particularly in the following aspects. First, the power supply system using solar panels needs to be established and it is necessary to ensure all sensor and gateway nodes can be supplied with more than 20% residuals during rainy or cloudy days. Second, for remote control of the installed sensors, an XML file is needed to have sending and editing functions, aiming at an adjustment of sensor parameters through the client server. Third, in case of data lost, it is crucial to establish a VPN transferring route between the local data center in Taziping and the monitoring headquarters in Shanghai, to ensure the safety of data security and data transfer. Fourth, a synchronization approach using GNSS should be tested so as to ensure that the synchronization rate is within 0.1 ms. Finally, when there is network congestion, the priority of data transfer needs to be defined with a first consideration of critical sensors relating to monitoring of the mass movement.

8. Conclusions

In this study, a systematic approach to landslide investigation based on remote sensing and Sensor Network (SN) has been developed and assessed. This approach is composed of three parts, landslide susceptibility mapping for susceptible spots determination in Hongkou Town (Sichuan, China),

scaled-down landslide simulation for SN prototype system test on the campus of Tongji University (Shanghai, China), and *in situ* SN design for field landslide observation at the Taziping landslide, Hongkou Town. First, the landslides triggered by the 2008 Wenchuan Earthquake were extracted by means of an object-oriented method from a pair of geo-referenced pre- and post- event IKONOS images (3.25 km² of landslide area compared with the 30 km² study site), followed by the correlation analysis between the landslide distribution and the control factors generated by DEM and vector data. The landslide susceptibility map was then produced by the Artificial Neural Network (ANN) algorithm to determine the susceptible landslide spots, and the Taziping landslide was selected for further investigation and SN deployment. Second, the SN was tested on a scaled-down landslide simulation platform before the *in situ* deployment to examine the usability of the sensors as well as the deployment strategy. Finally, the considerations and suggestions were given for the future *in situ* SN deployment in Taziping.

The research results support the following conclusions:

- (1) The spatial distribution of earthquake-triggered landslides is found to correlate with some of the control factors, e.g., it has positive correlation with the slope and seismic intensity factors, and the landslides occurred more easily in valleys with flowing rivers as well as within 200-to-500 m distance to roads.
- (2) The ANN is proved to be effective for generation of landslide susceptibility map to identify the zones of high risk. Correspondences of estimated susceptible areas compared with landslides extracted from the high-resolution IKONOS images were found in 89% of the cases.
- (3) The landslide simulation experiment demonstrates the applicability of the *in situ* sensors and SN in real-time landslide monitoring triggered by rainfall, and the potential for detection of early-warning signals useful for landslide prediction before the slope failure (e.g., 10 to 20 min in advance).
- (4) The integration of remote sensing approach and SN technique contributes to landslide research by bridging the gaps between large-scale regional landslide investigation and small-scale individual landslide monitoring, allowing the localization of slopes with higher hazard-risk probability for intensified and real-time landslide observation with deployment of SN.

Despite the achievements in this research, there are currently several limitations that need further improvement in the future. For example, the relatively short pre-alerting time requires the use of real-time data collection, communication and analysis to be exploited in the monitoring system for the deployment of SN in Taziping. Due to scale differences and field conditions between the simulation platform and the slope in Taziping, further tests in the field are required for real-scene landslide monitoring. Finally, the proposed methodology suffers from approximations entailed in the scaled-down models. These approximations, which however would be involved in any other modeling techniques (e.g., in numerical or empirical modeling), call for a careful validation with respect to observations collected from the real landslide in the future.

Acknowledgements

This study is supported by the National High Technology Research and Development Program of China (2012AA121302), the State Key Development Program for Basic Research of China

(2012CB957701, 2013CB733204 and 2013CB733203), the National Science Foundation of China (41201425, 41201424, and 41101443), the Key Laboratory of Advanced Engineering Surveying of SBSM (TJES0905) and the Key Laboratory of Mapping from Space of SBSM (K201005), and the Key Laboratory for Land Environment and Disaster Monitoring of SBSM (LEDM2009B02). The authors would like to thank Leslie B. Smith from the Mapping and GIS Lab, OSU for her English editing of the manuscript, and the anonymous reviewers for their valuable comments and suggestions.

Conflicts of Interest

The authors declare no conflict of interest.

References

1. Schuster, R.L. Socioeconomic Significance of Landslides. In *Landslides: Investigation and Mitigation*; Turner, A.K., Schuster, R.L., Eds.; Transportation Research Board Special Report 247; National Academies Press: Washington, DC, USA, 1996; pp. 12–35.
2. Sassa, K.; Tsuchiya, S.; Ugai, K.; Wakai, A.; Uchimura, T. Landslides: A review of achievements in the first 5 years (2004–2009). *Landslides* **2009**, *6*, 275–286.
3. Delacourt, C.; Allemand, P.; Berthier, E.; Raucoules, D.; Casson, B.; Grandjean, P.; Pambrun, C.; Varel, E. Remote-sensing techniques for analysing landslide kinematics: A review. *Bull. Soc. Géol. Fr.* **2007**, *178*, 89–100.
4. Metternicht, G.; Hurni, L.; Gogu, R. Remote sensing of landslides: An analysis of the potential contribution to geo-spatial systems for hazard assessment in mountainous environments. *Remote Sens. Environ.* **2005**, *98*, 284–303.
5. Guzzetti, F.; Mondini, A.C.; Cardinali, M.; Fiorucci, F.; Santangelo, M.; Chang, K.-T. Landslide inventory maps: New tools for an old problem. *Earth Sci. Rev.* **2012**, *112*, 42–66.
6. Tung, S.-H.; Shih, M.-H.; Sung, W.-P. Identification of the landslide using the satellite images and the digital image correlation method. *Disa. Adv.* **2013**, *6*, 4–9.
7. Van Westen, C.J.; Castellanos, E.; Kuriakose, S.K. Spatial data for landslide susceptibility, hazard, and vulnerability assessment: An overview. *Eng. Geol.* **2008**, *102*, 112–131.
8. Felicísimo, M.Á.; Cuartero, A.; Remondo, J.; Quirós, E. Mapping landslide susceptibility with logistic regression, multiple adaptive regression splines, classification and regression trees, and maximum entropy methods: A comparative study. *Landslides* **2013**, *10*, 175–189.
9. Strozzi, T.; Ambrosi, C.; Raetzo, H. Interpretation of aerial photographs and satellite SAR interferometry for the inventory of landslides. *Remote Sens.* **2013**, *5*, 2554–2570.
10. Chauhan, S.; Sharma, M.; Arora, K.M. Landslide susceptibility zonation of the Chamoli region, Garhwal Himalayas, using logistic regression model. *Landslides* **2010**, *7*, 411–423.
11. Park, S.; Chio, C.; Kim, B.; Kim, J. Landslide susceptibility mapping using frequency ratio, analytic hierarchy process, logistic regression, and artificial neural network methods at the Inje area, Korea. *Environ. Earth Sci.* **2013**, *68*, 1443–1464.
12. Tofani, V.; Raspini, F.; Catani, F.; Casagli, N. Persistent Scatterer Interferometry (PSI) technique for landslide characterization and monitoring. *Remote Sens.* **2013**, *5*, 1045–1065.

13. Mantovani, F.; Soeters, R.; van Westen, C.J. Remote sensing techniques for landslide studies and hazard zonation in Europe. *Geomorphology* **1996**, *15*, 213–225.
14. Dunning, S.A.; Rosser, N.J.; Massey, C.I. The integration of terrestrial laser scanning and numerical modeling in landslide investigations. *Q. J. Eng. Geol. Hydrogeol.* **2010**, *43*, 233–247.
15. Gigli, G.; Fanti, R.; Canuti, P.; Casagli, N. Integration of advanced monitoring and numerical modeling techniques for the complete risk scenario analysis of rockslides: The case of Mt. Beni (Florence, Italy). *Eng. Geol.* **2011**, *120*, 48–59.
16. Li, R. The CSISSD Research Team. Advanced Spatial Sensor Network Systems—Review, Status, and Applications. In Proceedings of 2011 International Symposium on Image and Data Fusion, Tengchong, Yunnan, China, 9–11 August 2011.
17. Ramesh, M.V. Design, development, and deployment of a wireless sensor network for detection of landslides. *Ad Hoc Netw.* **2012**, doi: 10.1016/j.adhoc.2012.09.002.
18. Arattano, M.; Marchi, L. Systems and sensors for debris-flow monitoring and warning. *Sensors* **2008**, *8*, 2436–2452.
19. Angeli, M.; Pasuto, A.; Silvano, S. A critical review of landslide monitoring experiences. *Eng. Geol.* **2000**, *55*, 133–147.
20. Akbarimehr, M.; Motagh, M.; Haghshenas-Haghighi, M. Slope stability assessment of the Sarcheshmeh Landslide, Northeast Iran, investigated using InSAR and GPS observations. *Remote Sens.* **2013**, *5*, 3681–3700.
21. Jaboyedoff, M.; Oppikofer, T.; Abellán, A.; Derron, M.H.; Loye, A.; Metzger, R.; Pedrazzini, A. Use of LIDAR in landslide investigations: A review. *Nat. Hazards* **2012**, *61*, 1–24.
22. Lato, M.J.; Bevan, G.; Fergusson, M. Gigapixel imaging and photogrammetry: Development of a new long range remote imaging technique. *Remote Sens.* **2012**, *4*, 3006–3021.
23. del Ventisette, C.; Ciampalini, A.; Manunta, M.; Calò, F.; Paglia, L.; Ardizzone, F.; Mondini, A.C.; Reichenbach, P.; Mateos, R.M.; Bianchini, S.; *et al.* Exploitation of large archives of ERS and ENVISAT C-Band SAR data to characterize ground deformations. *Remote Sens.* **2013**, *5*, 3896–3917.
24. Ou, J.; Qiao, G.; Bao, F.; Wang, W.; Di, K.; Li, R. A new method for automatic large scale map updating using mobile mapping imagery. *Photogramm. Rec.* **2013**, *28*, 240–260.
25. Sato, H.P.; Harp, E.L. Interpretation of earthquake-induced landslides triggered by the 12 May 2008, M7.9 Wenchuan earthquake in the Beichuan area, Sichuan Province, China, using satellite imagery and Google Earth. *Landslides* **2009**, *6*, 153–159.
26. Bozzano, F.; Cipriani, I.; Mazzanti, P.; Prestininzi, A. Displacement patterns of a landslide affected by human activities: Insights from ground-based InSAR monitoring. *Nat. Hazards* **2011**, *59*, 1377–1396.
27. Hong, Y.; Adler, R.F. Towards an early-warning system for global landslides triggered by rainfall and earthquake. *Int. J. Remote. Sens.* **2007**, *28*, 3713–3719.
28. Cruden, D.M.; Varnes, D.J. Landslides Types and Processes. In *Landslides: Investigation and Mitigation*; Turner, A.K., Schuster, R.L., Eds.; Transportation Research Board Special Report 247, National Academies Press: Washington, DC, USA, 1996; pp. 36–75.

29. Guzzetti, F.; Carrara, A.; Cardinali, M.; Reichenbach, P. Landslide hazard evaluation: A review of current techniques and their application in a multi-scale study, Central Italy. *Geomorphology* **1999**, *31*, 181–216.
30. Dai, F.C.; Lee, C.F.; Nhai, Y.Y. Landslide risk assessment and management: An overview. *Eng. Geol.* **2002**, *64*, 65–87.
31. Dai, F.C.; Xu, C.; Yao, X.; Xu, L.; Tu, X.B.; Gong, Q.M. Spatial distribution of landslides triggered by the 2008 Ms 8.0 Wenchuan Earthquake, China. *J. Asian Earth Sci.* **2011**, *40*, 883–895.
32. Tang, C.; Zhu, J.; Qi, X.; Ding, J. Landslides induced by the Wenchuan earthquake and the subsequent strong rainfall event: A case study in the Beichuan area of China. *Eng. Geol.* **2011**, *122*, 22–33.
33. Scaioni, M.; Lu, P.; Chen, W.; Qiao, G.; Wu, H.; Feng, T.; Tong, X.; Wang, W.; Li, R. Analysis of spatial sensor network observations during landslide simulation experiments. *Eur. J. Environ. Civil. Eng.* **2013**, doi: 10.1080/19648189.2013.822427.
34. Qi, S.W.; Xu, Q.; Lan, H.X.; Zhang, B.; Liu, J.Y. Spatial distribution analysis of landslides triggered by 2008.5.12 Wenchuan Earthquake, China. *Eng. Geol.* **2010**, *116*, 95–108.
35. Wang, F.W.; Cheng, Q.G.; Highland, L.; Miyajima, M.; Wang, H.B.; Yan, C.G. Preliminary investigation of some large landslides triggered by the 2008 Wenchuan earthquake, Sichuan Province, China. *Landslides* **2009**, *6*, 47–54.
36. Qiao, G.; Wang, W.; Wu, B.; Liu, C.; Li, R. Assessment of geo-positioning capability of high-resolution satellite imagery for densely populated high buildings in metropolitan areas. *Photogramm. Eng. Remote. Sens.* **2010**, *76*, 923–934.
37. Lu, P.; Stumpf, A.; Kerle, N.; Casagli, N. Object-oriented change detection for landslide rapid mapping. *IEEE Geosci. Remote Sens.* **2011**, *8*, 701–705.
38. Hölbling, D.; Füreder, P.; Antolini, F.; Cigna, F.; Casagli, N.; Lang, S. A semi-automated object-based approach for landslide detection validated by Persistent Scatterer Interferometry measures and landslide inventories. *Remote Sens.* **2012**, *4*, 1310–1336.
39. Yang, C.J.L.; Ren, X.L.; Huang, H. The vegetation damage assessment of the Wenchuan earthquake of May 2008 using remote sensing and GIS. *Nat. Hazards* **2012**, *62*, 45–55.
40. Lacroix, P.; Zavala, B.; Berthier, E.; Audin, L. Supervised method of landslide inventory using panchromatic SPOT5 images and application to the earthquake-triggered landslides of Pisco (Peru, 2007, Mw8.0). *Remote Sens.* **2013**, *5*, 2590–2616.
41. Defries, S.R.; Townshend, J.R.G. NDVI-derived land cover classifications at a global scale. *Int. J. Remote Sens.* **1994**, *15*, 3567–3586.
42. Marqués, F.; Gasull, A. *Multiresolution Image Segmentation Based on Compound Random Fields: Application to Image Coding*; Universitat Politècnica de Catalunya: Barcelona, Spain, 1992; pp. 86–114.
43. Tong, H.J.; Maxwell, T.; Zhang, Y.; Dey, V. A supervised and fuzzy-based approach to determine optimal multi-resolution image segmentation parameters. *Photogramm. Eng. Remote. Sens.* **2012**, *78*, 1029–1044.

44. Gorum, T.; Fan, X.M.; van Westen, J.C.; Huang, R.Q.; Xu, Q.; Tang, C.; Wang, G.H. Distribution pattern of earthquake-induced landslides triggered by the 12 May 2008 Wenchuan earthquake. *Geomorphology* **2011**, *133*, 152–167.
45. Conoscenti, C.; Maggio, C.D.; Rotigliano, E. GIS analysis to assess landslide susceptibility in a fluvial basin of NW Sicily (Italy). *Geomorphology* **2008**, *94*, 325–339.
46. Neuhäuser, B.; Damm, B.; Terhorst, B. GIS-based assessment of landslide susceptibility on the base of the Weights-of-Evidence model. *Landslides* **2012**, *9*, 511–528.
47. Pareek, N.; Sharma, M.L.; Arora, K.M. Impact of seismic factors on landslide susceptibility zonation: A case study in part of Indian Himalayas. *Landslides* **2010**, *7*, 191–201.
48. Chen, H.; Lin, G.W.; Lu, M.H.; Shih, T.Y.; Horng, M.J.; Wu, S.J.; Chuang, B. Effects of topography, lithology, rainfall and earthquake on landslide and sediment discharge in mountain catchments of southeastern Taiwan. *Geomorphology* **2011**, *133*, 132–142.
49. Akgun, A. A comparison of landslide susceptibility maps produced by logistic regression, multi-criteria decision, and likelihood ratio methods: A case study at İzmir, Turkey. *Landslides* **2012**, *9*, 93–106.
50. Othman, A.A.; Gloaguen, R. River courses affected by landslides and implications for hazard assessment: A high resolution remote sensing case study in NE Iraq–W Iran. *Remote Sens.* **2013**, *5*, 1024–1044.
51. Moreiras, S.M. Landslide susceptibility zonation in the Rio Mendoza Valley, Argentina. *Geomorphology* **2005**, *66*, 345–357.
52. Akgun, A.; Dag, S.; Bulut, F. Landslide susceptibility mapping for a landslide-prone area (Findikli, NE of Turkey) by likelihood-frequency ratio and weighted linear combination models. *Environ. Geol.* **2008**, *54*, 1127–1143.
53. Ray, R.L.; Jacobs, J.M.; Cosh, M.H. Landslide susceptibility mapping using downscaled AMSR-E soil moisture: A case study from Cleveland Corral, California, US. *Remote Sens. Environ.* **2010**, *114*, 2624–2636.
54. Bartlett, E.B. A stochastic training algorithm for artificial neural networks. *Neurocomputing* **1994**, *6*, 31–43.
55. Li, Y.; Chen, G.; Tang, C.; Zhou, G.; Zheng, L. Rainfall and earthquake-induced landslide susceptibility assessment using GIS and Artificial Neural Network. *Nat. Hazard Earth Syst. Sci.* **2012**, *12*, 2719–2729.
56. Liu, C.; Li, W.; Wu, H.; Lu, P.; Sang, K.; Sun, W.; Chen, W.; Hong, Y.; Li, R. Susceptibility evaluation and mapping of China's landslides based on multi-source data. *Nat. Hazards* **2013**, doi: 10.1007/s11069-013-0759-y.
57. Holmstrom, L.; Koistinen, P. Using additive noise in back-propagation training. *IEEE Trans. Neural Netw.* **1992**, *3*, 24–38.
58. Haykin, S. *Neural Networks: A Comprehensive Foundation*, 2nd ed.; Prentice-Hall: Upper Saddle River, NJ, USA, 1999; p. 823.
59. Ma, C.F.; Jiang, L.H. Some research on Levenberg–Marquardt method for the nonlinear equations. *Appl. Math. Comput.* **2007**, *184*, 1032–1040.

60. Lee, S.; Ryu, J.H.; Kim, L.S. Landslide susceptibility analysis and its verification using likelihood ratio, logistic regression, and artificial neural network models: Case study of Youngin, Korea. *Landslides* **2007**, *4*, 327–338.
61. OTEC Communication Technology Co. (Guangzhou, China). Available online <http://www.cnotec.cn/1234/html/?18.html> (assessed on 3 September 2013).
62. Sansoni, G.; Trebeschi, M.; Docchio, F. State-of-the-art and applications of 3D imaging sensors in industry, cultural heritage, medicine, and criminal investigation. *Sensors* **2009**, *9*, 568–601.
63. NOAA National Weather Service. Available online <http://mag.ncep.noaa.gov/> (accessed on 3 September 2013).
64. Casagli, N.; Catani, F.; del Ventisette, C.; Luzi, G. Monitoring, prediction, and early warning using ground-based radar interferometry. *Landslides* **2010**, *7*, 291–301.
65. Tapete, D.; Casagli, N.; Luzi, G.; Fanti, R.; Gigli, G.; Leva, D. Integrating radar and laser-based remote sensing techniques for monitoring structural deformation of archaeological monuments. *J. Archaeol. Sci.* **2013**, *40*, 176–189.
66. Heritage, G.L.; Large, A.R.G. *Laser Scanning for the Environmental Sciences*; John Wiley & Sons: Chichester, UK, 2009; p. 302.
67. Vosselman, G.; Maas, H.G. *Airborne and Terrestrial Laser Scanning*; Taylor and Francis Group: Boca Raton, FL, USA, 2010; p. 320.
68. Eisenbeiss, H.; Sauerbier, M. Investigation of UAV systems and flight modes for photogrammetric applications. *Photogramm. Rec.* **2011**, *26*, 400–421.
69. Tapete, D.; Fanti, R.; Cecchi, R.; Petrangeli, P.; Casagli, N. Satellite radar interferometry for monitoring and early-stage warning of structural instability in archaeological sites. *J. Geophys. Eng.* **2012**, *9*, S10–S25.

© 2013 by the authors; licensee MDPI, Basel, Switzerland. This article is an open access article distributed under the terms and conditions of the Creative Commons Attribution license (<http://creativecommons.org/licenses/by/3.0/>).